



**HAL**  
open science

# Absorption of Millimeter-band CO and CN in the Early Universe: Molecular Clouds in Radio Galaxy B2 0902+34 at Redshift 3.4

Bjorn Emonts, Steve Curran, George Miley, Matthew Lehnert, Chris Carilli, Ilsang Yoon, Raffaella Morganti, Reinout van Weeren, Montserrat Villar-Martin, Pierre Guillard, et al.

► **To cite this version:**

Bjorn Emonts, Steve Curran, George Miley, Matthew Lehnert, Chris Carilli, et al.. Absorption of Millimeter-band CO and CN in the Early Universe: Molecular Clouds in Radio Galaxy B2 0902+34 at Redshift 3.4. *Astrophys.J.*, 2024, 962 (2), pp.187. 10.3847/1538-4357/ad198d . hal-04416870

**HAL Id: hal-04416870**

**<https://hal.science/hal-04416870>**

Submitted on 19 Apr 2024

**HAL** is a multi-disciplinary open access archive for the deposit and dissemination of scientific research documents, whether they are published or not. The documents may come from teaching and research institutions in France or abroad, or from public or private research centers.

L'archive ouverte pluridisciplinaire **HAL**, est destinée au dépôt et à la diffusion de documents scientifiques de niveau recherche, publiés ou non, émanant des établissements d'enseignement et de recherche français ou étrangers, des laboratoires publics ou privés.



Distributed under a Creative Commons Attribution 4.0 International License



# Absorption of Millimeter-band CO and CN in the Early Universe: Molecular Clouds in the Radio Galaxy B2 0902+34 at Redshift 3.4

Bjorn H. C. Emonts<sup>1</sup> , Steve J. Curran<sup>2</sup> , George K. Miley<sup>3</sup> , Matthew D. Lehnert<sup>4</sup> , Chris L. Carilli<sup>5</sup> , Ilsang Yoon<sup>1</sup> , Raffaella Morganti<sup>6,7</sup> , Reinout J. van Weeren<sup>3</sup> , Montserrat Villar-Martín<sup>8</sup> , Pierre Guillard<sup>9</sup> , Cristina M. Cordun<sup>6,7</sup> , and Tom A. Oosterloo<sup>6,7</sup>

<sup>1</sup> National Radio Astronomy Observatory, 520 Edgemont Road, Charlottesville, VA 22903, USA; [bemonts@nrao.edu](mailto:bemonts@nrao.edu)

<sup>2</sup> School of Chemical and Physical Sciences, Victoria University of Wellington, P.O. Box 600, Wellington 6140, New Zealand

<sup>3</sup> Leiden Observatory, Leiden University, P.O. Box 9513, 2300 RA Leiden, The Netherlands

<sup>4</sup> Université Lyon 1, ENS de Lyon, CNRS UMR5574, Centre de Recherche Astrophysique de Lyon, F-69230 Saint-Genis-Laval, France

<sup>5</sup> National Radio Astronomy Observatory, P.O. Box O, Socorro, NM 87801, USA

<sup>6</sup> ASTRON, the Netherlands Institute for Radio Astronomy, Oude Hoogeveensedijk 4, 7991 PD Dwingeloo, The Netherlands

<sup>7</sup> Kapteyn Astronomical Institute, University of Groningen, P.O. Box 800, 9700 AV Groningen, The Netherlands

<sup>8</sup> Centro de Astrobiología, CSIC-INTA, Ctra. de Torrejón a Ajalvir, km 4, E-28850 Torrejón de Ardoz, Madrid, Spain

<sup>9</sup> Sorbonne Université, CNRS UMR 7095, Institut d'Astrophysique de Paris, 98bis bd Arago, F-75014 Paris, France

Received 2023 September 25; revised 2023 December 22; accepted 2023 December 27; published 2024 February 20

## Abstract

Using the Karl G. Jansky Very Large Array, we have detected absorption lines due to carbon monoxide, CO( $J=0 \rightarrow 1$ ), and the cyano radical, CN( $N=0 \rightarrow 1$ ), associated with radio galaxy B2 0902+34 at redshift  $z=3.4$ . The detection of millimeter-band absorption observed 1.5 Gyr after the Big Bang facilitates studying molecular clouds down to gas masses inaccessible to emission-line observations. The CO absorption in B2 0902+34 has a peak optical depth of  $\tau \geq 8.6\%$  and consists of two components, one of which has the same redshift as previously detected 21 cm absorption of neutral hydrogen (HI) gas. Each CO component traces an integrated H<sub>2</sub> column density of  $N_{\text{H}_2} \gtrsim 3 \times 10^{20} \text{ cm}^{-2}$ . CN absorption is detected for both CO components, as well as for a blueshifted component not detected in CO, with CO/CN line ratios ranging from  $\lesssim 0.4$  to 2.4. We discuss the scenario that the absorption components originate from collections of small and dense molecular clouds that are embedded in a region with more diffuse gas and high turbulence, possibly within the influence of the central active galactic nucleus or a starburst region. The degree of reddening in B2 0902+34, with rest-frame color  $B - K \sim 4.2$ , is lower than the very red colors ( $B - K > 6$ ) found among other known redshifted CO absorption systems at  $z < 1$ . Nevertheless, when including the many nondetections from the literature, a potential correlation between the absorption-line strength and  $B - K$  color is evident, giving weight to the argument that the red colors of CO absorbers are due to a high dust content.

*Unified Astronomy Thesaurus concepts:* [Radio spectroscopy \(1359\)](#); [Galaxy jets \(601\)](#); [Quasar absorption line spectroscopy \(1317\)](#); [Extinction \(505\)](#); [Cosmological parameters \(339\)](#); [Radio sources \(1358\)](#); [Molecular clouds \(1072\)](#); [Galaxy evolution \(594\)](#)

## 1. Introduction

Radio synchrotron jets emanating from active black holes are sources of bright continuum emission, which can act as background candles that facilitate the search for spectral lines in absorption at centimeter and millimeter wavelengths. As a result, radio absorption lines have provided a diagnostic for studying neutral and molecular gas clouds along our line of sight toward radio sources (see the reviews by Combes 2008; Morganti & Oosterloo 2018).

Studies of molecular absorbers at low and intermediate redshifts provided insight into the raw materials that fuel early star formation and active galactic nucleus (AGN) activity (e.g., Gerin et al. 1997; Wiklind & Combes 1999; Maccagni et al. 2018; Wiklind et al. 2018; Allison et al. 2019; Combes et al. 2019; Rose et al. 2019; Morganti et al. 2023; Rose et al. 2023). In addition, they have been used to study extragalactic chemistry (e.g., Combes & Wiklind 1997; Muller et al. 2011, 2014), time

variability in the background radio source (e.g., Muller et al. 2023), the temperature of the cosmic microwave background (CMB; e.g., Muller et al. 2013; Riechers et al. 2022), and potential spacetime variations of fundamental constants (e.g., Carilli et al. 2000; Curran et al. 2011a; Muller et al. 2021). When extended to higher redshifts, such studies could provide critical new insights into physical processes that govern cosmology and galaxy evolution in the early Universe. Moreover, the strength of the absorption signal scales with the flux of the background radio continuum, and not directly with luminosity distance. This means that absorption lines have the potential to trace molecular clouds in the early Universe down to gas masses that cannot be detected with emission-line observations, considering that even the most detailed high- $z$  emission-line studies only resolve molecular clumps containing millions to billions of solar masses of cold gas (see, e.g., Hodge et al. 2012; Dessauges-Zavadsky et al. 2023).

To date, molecular hydrogen absorption has been detected in over 30 damped Ly $\alpha$  systems at high redshifts (e.g., Levshakov & Varshalovich 1985; Balashev et al. 2014; Noterdaeme et al. 2015; Balashev & Noterdaeme 2018; Ranjan et al. 2018). However, in the millimeter regime, when it comes to lines of sight against discrete and typically strong background

continuum sources, redshifted molecular absorption is rare; to date, CO had only been detected along six sight-lines at  $z_{\text{abs}} \gtrsim 0.1$ , all of which were at  $z_{\text{abs}} \leq 0.89$  (Wiklind & Combes 1995, 1996b, 1997, 1998; Wiklind et al. 2018; Allison et al. 2019).<sup>10</sup> This is despite extensive millimeter-band searches, both targeted (Wiklind & Combes 1995, 1996a; Drinkwater et al. 1996; Murphy et al. 2003; Curran et al. 2008, 2011b) and untargeted (Kanekar et al. 2014; Klitsch et al. 2019).<sup>11</sup> A new study by Combes & Gupta (2024) reports the detection of three new CO absorbers, two at  $z_{\text{abs}} \approx 1.2$  and one at  $z_{\text{abs}} = 3.387$ .<sup>12</sup> The latter is an intervening absorber tentatively detected at  $\sim 3\sigma$ , near the redshift of HI absorption detected by Kanekar et al. (2007).

Here we present the detection of molecular absorption associated with the high-redshift radio galaxy B2 0902+34 at  $z = 3.396$ . B2 0902+34 was one of the first galaxies discovered in the early Universe, thanks to its bright radio continuum, which served as a beacon for tracing the faint host galaxy (Lilly 1988; Eisenhardt & Dickinson 1992). It was suggested that this is a protogalaxy undergoing its first episode of star formation (Eales et al. 1993; Pentericci et al. 1999). X-ray observations revealed that it contains a heavily obscured AGN (Fabian et al. 2002). Carilli (1995) described the radio/optical structure of this galaxy as “bizarre,” with a bright northern radio lobe that shows a sharp ( $\sim 90^\circ$ ) bend and a flat-spectrum radio core located in a “valley” between two optical peaks. Recent 144 MHz imaging of the radio source with the Low Frequency Array (LOFAR) suggests that the complex radio structure is either the result of different episodes of AGN activity, or, more likely, due to interactions between the radio source and the surrounding halo gas (Cordun et al. 2023). B2 0902+34 is surrounded by a rich circumgalactic medium (CGM) in the form of a giant Ly $\alpha$  nebula (Reuland et al. 2003), and is thought to be a collapsing protogiant elliptical (Adams et al. 2009). Searches for molecular gas using CO(4–3) emission were done only using single-dish telescopes, which set limits of  $M_{\text{H}_2} \lesssim 5 \times 10^{10} M_\odot$  (Evans et al. 1996; van Ojik et al. 1997). B2 0902+34 is exceptional in that it is one of the very few  $z > 2$  radio sources that has been observed to have an associated HI absorption line (Curran et al. 2008; see also Uson et al. 1991; Briggs et al. 1993; Cody & Braun 2003; Chandra et al. 2004). Here we show that B2 0902+34 also has molecular absorption lines corresponding to carbon monoxide, CO( $J=0 \rightarrow 1$ ), and the cyano radical, CN( $N=0 \rightarrow 1$ ). At  $z = 3.396$ , it is the highest-redshift CO absorber known to date.

Throughout this paper, we assume the following cosmological parameters:  $H_0 = 71 \text{ km s}^{-1} \text{ Mpc}^{-1}$ ,  $\Omega_M = 0.27$ , and  $\Omega_\Lambda = 0.73$  (Wright 2006). The corresponding angular scale is  $7''.3$  kpc per arcsecond.

## 2. Data

The observations of B2 0902+34 were performed with NSF’s Karl G. Jansky Very Large Array (VLA) in D configuration under project 21A-059 during 2021 March 21–May 8. The total on-source time was 18.7 hr. We used a

<sup>10</sup> Apart from this, the highest-redshift detection is absorption by H<sub>2</sub>O at  $z_{\text{abs}} = 6.34$  against the CMB background with the Atacama Large Millimeter/submillimeter Array (ALMA; Riechers et al. 2022).

<sup>11</sup> The work by Klitsch et al. (2019) is based on ALMA calibration data from Oteo et al. (2016).

<sup>12</sup> Combes & Gupta (2024) also report the detection of an HNC absorber at  $z_{\text{abs}} \approx 1.3$ .

continuous bandwidth coverage of 1 GHz, consisting of 16 overlapping subbands of 128 MHz, with 1 MHz channels, centered around the redshifted CO( $J=0 \rightarrow 1$ ) line at 26.2 GHz ( $\nu_{\text{rest}} = 115.2712$  GHz). We observed the primary calibrator source J09027+3902 located at  $6''.5$  distance from B2 0902+34 every 5 min to calibrate the complex gains and bandpass. 3C 286 and 3C 147 were used for absolute flux calibration.

The data were processed using the Common Astronomy Software Applications (CASA; CASA Team et al. 2022), using version 6.4.3-27 during the calibration and 6.5.2-26 for the imaging. After a standard manual calibration, we self-calibrated the data using the unresolved radio-continuum source of B2 0902+34 to correct the complex gains further. We then imaged the radio continuum using the line-free channels and applying a natural weighting scheme, which resulted in a synthesized beam of  $3''.9 \times 3''.5$  (position angle of  $-12^\circ.1$ ). We also performed a deconvolution to clean the signal of the radio continuum. The radio continuum is unresolved and peaks at  $22.1 \pm 1.1 \text{ mJy beam}^{-1}$ .

For the line data, artifacts appeared at the level of a few percent, which is smaller than the assumed 5% uncertainty in the flux calibration of the VLA data. These artifacts are likely related to small variations in the point-spread function across the large fractional bandwidth of the data or inaccuracies in the relative calibration between the 16 subbands, combined with the limited spectral dynamic range reached by our observations (one in a few hundred). These artifacts scale with the brightness of the continuum emission. As a result, they become noticeable against the peak of the radio continuum as small (millijansky level) amplitude “jumps” along the bandpass. To mitigate this effect to a level that it does not affect the line data, we created a continuum-free ( $u, v$ ) data set prior to imaging the line data. For this, we used the continuum model that was derived during the deconvolution process of the continuum imaging, which we converted into model visibilities by applying a Fourier transform with the CASA task “ft.” These model visibilities were then subtracted from the ( $u, v$ ) data with the CASA task “uvsub.” Any residual continuum emission was subsequently subtracted in the ( $u, v$ ) domain using a linear fit to the line-free channels with the CASA task “uvcontsub.” Our CO( $J=0 \rightarrow 1$ ) absorption was well captured in a single subband, in a region of the spectrum that did not suffer from any of the artifacts that appeared prior to the continuum subtraction. This allowed us to verify that our continuum subtraction did not negatively affect the absorption signal (see Appendix A).

After subtracting the continuum, we imaged the line data using a natural weighting scheme and native  $11.9 \text{ km s}^{-1}$  channels, while cleaning the line signal in each channel until an absolute value for the threshold of  $0.35 \text{ mJy beam}^{-1}$  was reached. The rms noise of this image cube is  $\sigma = 0.05 \text{ mJy beam}^{-1} \text{ channel}^{-1}$ .

### 2.1. Hubble Space Telescope

We also obtained an image with the Hubble Space Telescope (HST) Wide Field Camera 3 (WFC3) in the F105W filter (project ID: 17268, PI: Emonts). The observations were executed on 2023 October 9, and the total on-source integration time was 37 minutes. The F105W filter is devoid of emission lines at the redshift of B2 0902+34 and traces the stellar continuum at 300 nm in the rest frame. We obtained the F105W image from the Multimission Archive at the Space Telescope Science Institute (MAST):[10.17909/cy88-7e89](https://archive.stsci.edu/missions/multiarchive/missions/10.17909/cy88-7e89). A

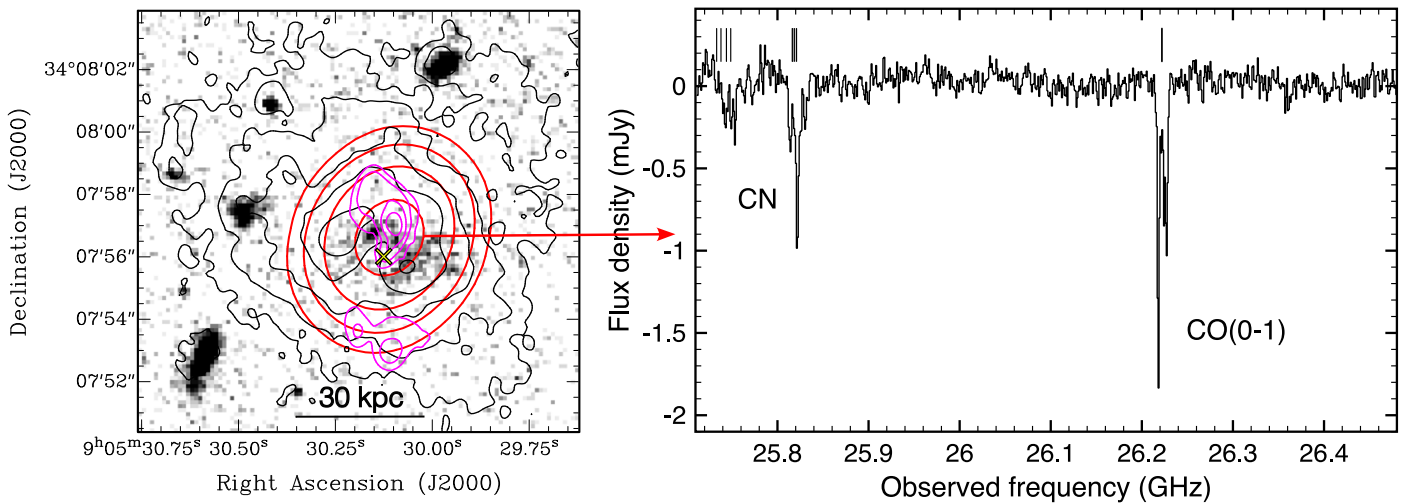


**Figure 1.** VLA observations of B2 0902+34. Left: HST WFC3/F105W image of B2 0902+34, with the contours of the unresolved continuum emission of our VLA D-configuration data overlaid in red and the 144 MHz LOFAR image from Cordun et al. (2023) overlaid in magenta contours. The contour levels of the VLA [LOFAR] data start at 2.2 [2.5] mJy beam<sup>-1</sup> and increase by a factor 2 [4]. The cross marks the location of the nucleus identified by Carilli (1995). We shifted the LOFAR data by  $\sim 0''.7$  to match this astrometry. The black contours represent the Ly $\alpha$  image from Reuland et al. (2003), with levels starting at 4% of the peak flux in the halo and increasing by a factor of 2. Right: Spectrum of B2 0902+34 taken against the unresolved VLA continuum. The flux density after continuum subtraction is plotted against the observed frequency. The small vertical bars above the spectrum indicate the redshift  $z = 3.3960$  for the CO( $J = 0 \rightarrow 1$ ) and two CN( $N = 0 \rightarrow 1$ ) lines, which in turn consist of a series of hyperfine lines.

detailed analysis of the HST imaging will be postponed to a future paper.

### 3. Results

Figure 1 shows the absorption spectrum taken against the radio continuum of B2 0902+34, where the lines of CO( $J = 0 \rightarrow 1$ ), CN( $N = 0 \rightarrow 1$ )  $J = 3/2 - 1/2$ , and CN( $N = 0 \rightarrow 1$ )  $J = 1/2 - 1/2$  are clearly evident. While the background continuum source has a total extent  $\sim 5''$  (Carilli 1995), the nucleus and brightest part of the northern lobe are unresolved in our D-configuration observations, while the faint southern radio lobe is not detected in our 26 GHz data. The peak flux density of this unresolved background continuum is  $22.1 \pm 1.1$  mJy beam<sup>-1</sup>.<sup>13</sup>

The HST WFC3/F105W image in Figure 1 (left) shows faint stellar light across a region  $\sim 30$  kpc, similar to the low surface brightness emission seen by Pentericci et al. (1999) in a bluer F622W ( $\lambda_{\text{rest}} \sim 180$  nm) image taken with the Wide Field and Planetary Camera 2. This optical emission is faintest at the location of the radio core, which could hint to the presence of large amounts of dust (see also Pentericci et al. 1999). However, the astrometry remains somewhat ambiguous, because all the radio maps relied on self-calibration, which leaves inherent astrometric errors (e.g., Pearson & Readhead 1984). A detailed discussion of the HST data will be given in a future paper.

#### 3.1. CO( $J = 0 \rightarrow 1$ ) Absorption

Figure 2 shows in detail the CO( $J = 0 \rightarrow 1$ ) absorption, which consists of two components (Table 1). We place the systemic redshift in the middle between the two components, namely  $z = 3.3960 \pm 0.0008$ . The uncertainty reflects the difference in redshift of the two CO components.

<sup>13</sup> The uncertainty is based on an assumed 5% uncertainty in the absolute flux calibration.

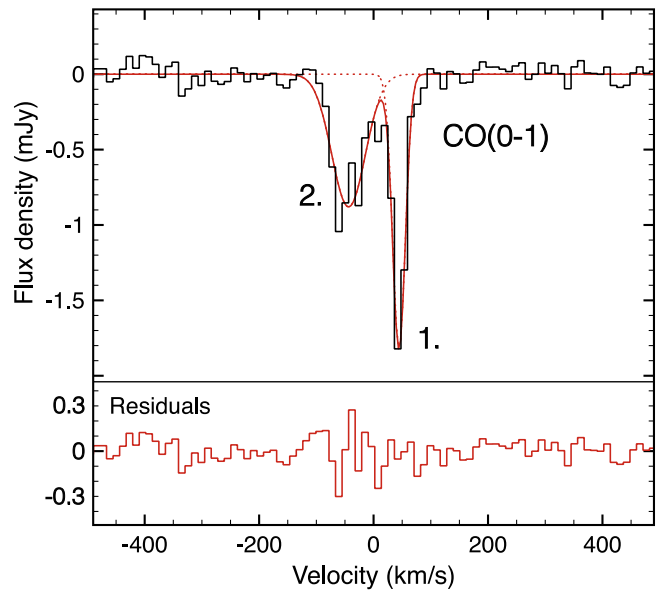


**Figure 2.** Spectrum of CO( $J = 0 \rightarrow 1$ ). The flux density after continuum subtraction is plotted against the radio velocity with respect to  $z = 3.3960$ . The red line shows a double Gaussian fit, where the dashed lines show the individual Gaussian components (indicated as 1 and 2, as per Table 1). The bottom panel shows the residuals after subtracting the fitted model from the spectrum.

The deep, narrow CO component has a redshift of  $z_{\text{CO}} = 3.3966 \pm 0.0001$ , which is in agreement with the redshift of  $z_{\text{HI}} = 3.3967 \pm 0.0002$  derived from HI 21 cm absorption of neutral hydrogen gas that was previously detected with the Giant Meterwave Radio Telescope (Chandra et al. 2004), as well as earlier detections with the VLA (Uson et al. 1991), the Arecibo telescope (Briggs et al. 1993), and the Westerbork Synthesis Radio Telescope (Cody & Braun 2003). This CO component has an  $\text{FWHM}_{\text{CO}} \approx 26$  km s<sup>-1</sup>, which is a factor 3 narrower than the FWHM of the HI absorber (Chandra et al. 2004). The optical depth of the narrow CO component is

**Table 1**  
Results of Gaussian Fitting to the Spectra

Line	Comp.	$z$	$v^a$ (km s $^{-1}$ )	FWHM $^b$ (km s $^{-1}$ )	$S_{\text{abs}}$ (mJy)	$\tau_{\text{obs}}^c$	$\int \tau_{\text{obs}} \delta v^d$ (km s $^{-1}$ )	CO/CN $^e$
CO( $J=0 \rightarrow 1$ )	1	$3.3966 \pm 0.0001$	$44 \pm 6$	$26 \pm 6$	$-1.82 \pm 0.12$	$0.086 \pm 0.007$	$2.98 \pm 0.73$	...
	2	$3.3953 \pm 0.0001$	$-44 \pm 6$	$69 \pm 8$	$-0.88 \pm 0.07$	$0.041 \pm 0.004$	$2.36 \pm 0.36$	...
CN( $N=0 \rightarrow 1$ )	1	$3.3965 \pm 0.0001$	$32 \pm 7$	$35 \pm 10$	$-0.33 \pm 0.07$	$0.015 \pm 0.003$	$1.24 \pm 0.45$	2.4
	2	$3.3952 \pm 0.0001$	$-57 \pm 6$	$32 \pm 7$	$-0.76 \pm 0.08$	$0.035 \pm 0.004$	$2.32 \pm 0.58$	1.0
	3	$3.3938 \pm 0.0001$	$-157 \pm 10$	$26 \pm 10$	$-0.23 \pm 0.07$	$0.010 \pm 0.003$	$0.66 \pm 0.33$	$\leq 0.4$

**Notes.** The uncertainties include uncertainties in the fitting, as well as half the width of the channel (for  $v$  and FWHM) and a 5% uncertainty in absolute flux calibration (for  $S_{\text{abs}}$ ). Uncertainties are added in quadrature and propagated for  $\tau$  and  $\int \tau_{\text{obs}} \delta v$ .

<sup>a</sup> Velocity is with respect to  $z = 3.3960$  ( $v = 0$  km s $^{-1}$ ).

<sup>b</sup> FWHM is the full width at half the maximum intensity.

<sup>c</sup> The observed optical depth,  $\tau_{\text{obs}}$ , is estimated using  $\tau_{\text{obs}} = -\ln\left(\frac{S_{\text{cont}} - S_{\text{abs}}}{S_{\text{cont}}}\right)$ . Because the background continuum is unresolved,  $\tau_{\text{obs}}$  represents the lower limit to the true optical depth,  $\tau$ .

<sup>d</sup> The observed integrated optical depth,  $\int \tau_{\text{obs}} \delta v$ , for CN reflects the combined value of all the hyperfine lines of the CN( $N=0 \rightarrow 1$ )  $J=3/2-1/2$  group. Following atomic physics, the integrated optical depth of the model fit to the  $1/2-1/2$  group was constrained to be a factor 0.61 lower than that of the  $3/2-1/2$  group. The contribution of the  $1/2-1/2$  group is not included in the above estimate of  $\int \tau_{\text{obs}} \delta v$  to facilitate easy comparison with results from the literature.

<sup>e</sup> The CO/CN line ratio is defined as the ratio of the integrated optical depths,  $\int \tau_{\text{CO,obs}} \delta v_{\text{CO}} / \int \tau_{\text{CN,obs}} \delta v_{\text{CN}}$ .

$\tau \gtrsim 8.6\%$ . Our observed optical depth is based on the unresolved background continuum at 26 GHz. Unless the absorption covers the background radio-continuum source uniformly, resolving the radio continuum at higher spatial resolution would decrease the flux density of the background continuum against which the absorption occurs. This is why our estimate of the observed optical depth  $\tau_{\text{obs}}$  is a lower limit to the true optical depth  $\tau$ .

A broader CO( $J=0 \rightarrow 1$ ) component is centered on a velocity of  $-88$  km s $^{-1}$  blueward of the narrow line, with  $\text{FWHM}_{\text{CO}} \approx 69$  km s $^{-1}$  and  $\tau \gtrsim 4.1\%$ . This CO component has no obvious counterpart in the HI 21 cm absorption spectra.

### 3.2. CN( $N=0 \rightarrow 1$ ) Absorption

CN( $N=0 \rightarrow 1$ ) consists of nine hyperfine lines in the VLA band, divided into two groups: the CN( $N=0 \rightarrow 1$ )  $J=3/2-1/2$  group has the highest integrated brightness and consists of five lines, one of which is too faint to be detected above the noise in our data. The fainter CN( $N=0 \rightarrow 1$ )  $J=1/2-1/2$  group consists of four lines. As shown in Figure 3, three components, representing three different absorbers, are required to obtain a good fit to the CN spectra. The fitting was performed with an unconstrained Gaussian fit to the brightest (hereafter “main”) hyperfine line for each of the three components of the stronger CN( $N=0 \rightarrow 1$ )  $J=3/2-1/2$  multiplet, while at the same time representing the other hyperfine lines with additional Gaussians that had their center, width, and intensity constrained to the main line as per atomic physics (Osterbrock 1989). The exact same solutions were applied to the hyperfine lines of the weaker CN( $N=0 \rightarrow 1$ )  $J=1/2-1/2$  multiplet, again constraining the center, width, and intensity based on atomic physics. Therefore, the fully constrained fit to the weaker CN( $N=0 \rightarrow 1$ )  $J=1/2-1/2$  multiplet merely serves to assure that our model accurately represents both CN multiplets (see Figure 3 for details).

The redshifts of components 1 and 2 are consistent to within one channel with the redshifts of the two CO( $J=0 \rightarrow 1$ ) absorbers (Figure 4). We therefore assume that the CN and CO absorptions originate from the same gas reservoir. Component

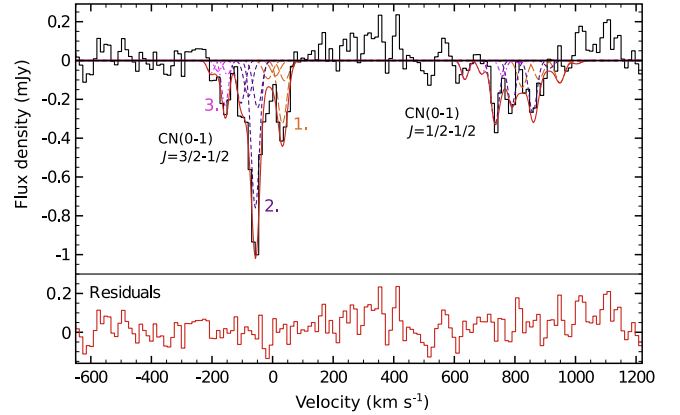


**Figure 3.** Spectrum of CN( $N=0 \rightarrow 1$ ). The flux density after continuum subtraction is plotted against the radio velocity of the stronger CN( $N=0 \rightarrow 1$ )  $J=3/2-1/2$  multiplet with respect to  $z = 3.3960$ . The red line shows a fitted model consisting of three components, with each component representing a CN absorber (the orange, purple, and magenta colors represent components 1, 2, and 3 from Table 1, respectively). Each component in turn consists of four Gaussians (visualized by the same color), which represent the four detectable hyperfine lines of each CN absorber. The bottom panel shows the residuals after subtracting the fitted model from the spectrum.

3 of CN is the weakest of the three and has no counterpart in CO( $J=0 \rightarrow 1$ ) at the detection limit of our data.

## 4. Discussion

### 4.1. Physical Properties of the Molecular Gas

The detection of both CO( $J=0 \rightarrow 1$ ) and CN( $N=0 \rightarrow 1$ ) in absorption allows us to derive physical properties of the absorbing gas. The ground-transition CO( $J=0 \rightarrow 1$ ) is the most reliable tracer for the overall molecular gas content across the full range of densities, independent of the excitation properties of the gas (e.g., Bolatto et al. 2013). In contrast, CN( $N=0 \rightarrow 1$ ) traces moderately dense ( $\gtrsim 10^4$  cm $^{-3}$ ) molecular gas (Brooke et al. 2014; Shirley 2015).

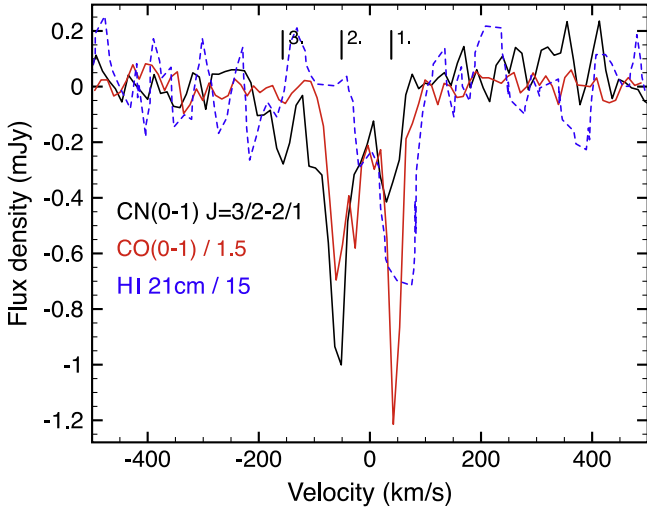


**Figure 4.** Overlay of CN( $N=0 \rightarrow 1$ )  $J=3/2-1/2$  (black line), CO( $J=0 \rightarrow 1$ ) (red line), and the H I 21 cm spectrum from Chandra et al. (2004; blue dashed line). For clarity, the CO( $1-0$ ) and H I spectra were scaled down by a factor of 1.5 and 15, respectively. The three components from Table 1 are indicated with the small vertical bars.

#### 4.1.1. Column Densities

To derive CO column densities, we follow Allison et al. (2019):<sup>14</sup>

$$N_{\text{CO}} \geq \frac{8\pi}{c^3} \frac{\nu^3}{g_{J+1}A_{J+1}} \frac{Q(T_{\text{ex}})e^{E_J/k_B T_{\text{ex}}}}{1 - e^{-h\nu/k_B T_{\text{ex}}}} \int \tau_{\text{CO}} \delta\nu, \quad (1)$$

where  $\nu$  is the CO( $J=0 \rightarrow 1$ ) rest frequency,  $g_{J+1}$  is the statistical weight for the upper ( $J+1=1$ ) energy level,  $A_{J+1} = 7.67 \times 10^{-8} \text{ s}^{-1}$  is the Einstein A coefficient (see Chandra et al. 1996),  $Q(T_{\text{ex}})$  is the partition function assuming a single excitation temperature  $T_{\text{ex}}$ ,  $E_J$  is the energy of the lower ( $J=0$ ) level, and  $\int \tau_{\text{CO}} \delta\nu$  is the optical depth integrated over the width of the absorption profile (from Table 1). The variables  $h$  and  $k_B$  are the Planck and Boltzmann constants, respectively. For CO, the rigid-rotor approximation allows us to use  $g_{J+1} = 2(J+1) + 1$ , and also approximate  $Q(T_{\text{ex}}) \approx T_{\text{ex}}/B$  (for  $T_{\text{ex}} \gg B$ ) and  $E_J/k_B \approx J(J+1)B$  (see Allison et al. 2019). Here,  $B = 2.766 \text{ K}$  is the rotational constant for CO. Furthermore, we assume  $T_{\text{ex}} \gtrsim 15 \text{ K}$  (e.g., Wilson et al. 1997). Higher values than the lower limit of 15 K are expected if the molecular gas is located in a star-forming region or in the vicinity of an AGN. The above parameters imply CO column densities of  $N_{\text{CO}} \geq 2.4 \times 10^{16} \text{ cm}^{-2}$  for the deep, narrow component, and  $N_{\text{CO}} \geq 3.1 \times 10^{16} \text{ cm}^{-2}$  for the broader CO component. We do not take into consideration potential line dimming as a result of the increased temperature of the CMB radiation at  $z=3.4$  (da Cunha et al. 2013; Zhang et al. 2016). This provides an additional reason for considering  $N_{\text{CO}}$  to be a lower limit.

If we assume a CO/H<sub>2</sub> abundance of  $1 \times 10^{-4}$  that was found for molecular clouds in the Milky Way (Frerking et al. 1982), then each component has a total H<sub>2</sub> column density of roughly  $N_{\text{H}_2} \gtrsim 3 \times 10^{20} \text{ cm}^{-2}$ .

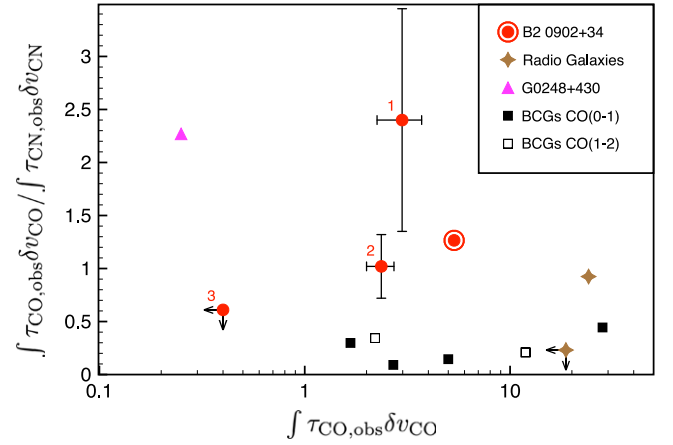


**Figure 5.** Ratio of the observed integrated optical depths ( $\int \tau_{\text{obs}} \delta\nu$ ) of CO( $J=0 \rightarrow 1$ ) and CN( $N=0 \rightarrow 1$ )  $J=3/2-1/2$ , plotted against the integrated optical depth of CO( $J=0 \rightarrow 1$ ). The circled red dot represents the average value for B2 0902+34, with the red dots showing the three individual components from Table 1. The other symbols represent low- $z$  systems: the brown stars are two radio galaxies, namely 4C 31.04 at  $z=0.06$  and upper limits for 4C 52.37 at  $z=0.1$  (Morganti et al. 2023; see also S. Murthy et al. 2024, in preparation); the magenta triangle is the merger system G0248+430 at  $z=0.05$  (Combes et al. 2019); and the squares represent BCGs at  $0.01 \lesssim z \lesssim 0.23$ , with the two open squares being BCGs observed in CO( $J=1 \rightarrow 2$ ) instead of CO( $J=0 \rightarrow 1$ ) (Rose et al. 2019).

#### 4.1.2. CN Abundance

The formation of CN occurs through several routes that take place simultaneously in molecular clouds, especially at the transition boundary from H I to H<sub>2</sub> in regions illuminated by UV radiation. These routes include photodissociation of HCN ( $\text{HCN} + \nu \rightarrow \text{CN} + \text{H}$ ), collisions with hydrogen atoms in high-density regions ( $\text{HCN} + \text{H} \rightarrow \text{CN} + \text{H}_2$ ), dissociative recombination ( $\text{HCN}^+ + e^- \rightarrow \text{CN} + \text{H}$ ), and chemistry in photodissociation regions (PDRs) at an extinction of  $A_V \sim 2 \text{ mag}$  ( $\text{N} + \text{C}_2 \rightarrow \text{CN} + \text{C}$  and  $\text{N} + \text{CH} \rightarrow \text{CN} + \text{H}$ ; e.g., Sternberg & Dalgarno 1995). This means that the CN abundance is enhanced in the outer regions of molecular clouds exposed to UV radiation fields in PDRs (e.g., Fuente et al. 1995; Aalto et al. 2002; Boger & Sternberg 2005), or in regions where the X-ray ionization rates are high (e.g., Lepp & Dalgarno 1996; Meijerink et al. 2007).

The observed ratios of the velocity-integrated optical depths of the CO( $J=0 \rightarrow 1$ ) and CN( $N=0 \rightarrow 1$ )  $J=3/2-1/2$  lines, or  $\int \tau_{\text{CO,obs}} \delta\nu_{\text{CO}} / \int \tau_{\text{CN,obs}} \delta\nu_{\text{CN}}$  (hereafter CO/CN), are CO/CN  $\sim 2.4$  for component 1, CO/CN  $\sim 1.0$  for component 2, and CO/CN  $\lesssim 0.4$  for component 3, with the latter assuming a CO( $J=0 \rightarrow 1$ ) nondetection of  $3\sigma$  across  $\text{FWHM}_{\text{CO}} \equiv \text{FWHM}_{\text{CN}} = 26 \text{ km s}^{-1}$  (see Table 1). As can be seen in Figure 5, the CO/CN value for component 1 is comparable to the absorption-line value from a tidal tail in the merger system G0248+430, which is illuminated by a background quasar (Combes et al. 2019). The CO/CN value for component 2 is similar to the value found in the low- $z$  radio galaxy 4C 31.04 (Morganti et al. 2023; see also S. Murthy et al. 2024, in preparation). Component 3 has a CO/CN limit comparable to the limit found for radio galaxy 4C 52.37 (Morganti et al. 2023). Given that B2 0902+34 is thought to be a collapsing protogiant elliptical (Adams et al. 2009), we also compare the CO/CN absorption values with those of a small sample of low- $z$  brightest cluster galaxies (BCGs) studied by Rose et al. (2019). These low- $z$  BCGs have CO/CN ratios in agreement

<sup>14</sup> See also Wiklind & Combes (1995), Wilson et al. (2013), Mangum & Shirley (2015), and Rose et al. (2019).

with the limit that we derive for component 3 in B2 0902+34, but lower than those of the main components 1 and 2.

When we compare our absorption results to emission-line studies, our CO/CN values are low compared to the emission-line ratios found for nearby galaxies (Wilson 2018) and luminous infrared galaxies (Aalto et al. 2002), which typically have  $\text{CO}/\text{CN} \gtrsim 10$ . However, our absorption results are comparable to the emission-line ratios found in the molecular outflow of Mrk 231 (Cicone et al. 2020), the circum-nuclear disk of the active galaxy NGC 1068 (García-Burillo et al. 2010), and the  $z \sim 2.56$  Cloverleaf quasar (Riechers et al. 2007). This suggests that the CN abundance is likely enhanced by a UV or X-ray radiation field, and may thus originate close to the central AGN region, which is designated as region “N” by Carilli (1995). In Mrk 231, the outflow component shows roughly  $4\times$  lower CO/CN ratios than the gas in the center of the host galaxy (Cicone et al. 2020). For absorption detections, any outflow would be aligned in front of the radio source, and thus be blueshifted. In this respect, it is interesting that the most blueshifted component in B2 0902+34 also has the lowest CO/CN value. However, regarding all the above, we note that a one-on-one comparison between emission- and absorption-line studies may be limited by density and beam-filling effects. Moreover, the CN abundance is very sensitive to the fraction of mechanical energy in photon-dominated regions (Kazandjian et al. 2015).

Alternatively, Morganti et al. (2023) discuss that CN can be enhanced relative to CO in low-density, irradiated molecular shocks (Godard et al. 2019; Lehmann et al. 2022), or diffuse molecular gas with a high velocity dispersion (Wakelam et al. 2015). The CO/CN values that we find in B2 0902+34 resemble those found in the low- $z$  radio galaxies 4C 31.04 and 4C 52.37 by Morganti et al. (2023; Figure 5). This could be consistent with the scenario that the radio source interacts with the surrounding gaseous medium (Cordun et al. 2023; see Section 1).

In future work we will further address the nature of the CN absorption by studying the location of the absorption components, and targeting other dense molecular gas tracers such as HCN and  $\text{HCO}^+$ .

#### 4.1.3. Cloudy Gas Reservoir

The properties of the molecular gas reservoirs that cause the absorption features along the line of sight toward the radio continuum depend on whether the gas is part of the interstellar medium (ISM) close to the AGN, the ISM further out in the host galaxy, or the large-scale CGM. We will address this with future observations at higher spatial resolution, which will resolve the background continuum and therefore identify the location of the absorption components. For the moment, we will follow the assumption made in Section 4.1.2 that the molecular gas is part of the ISM, possibly near the AGN. We also follow Guszejnov et al. (2020), who show that the properties of molecular clouds (mass, velocity dispersion, and volume density) do not significantly change from redshift 4 to 0. The discussion in this section will focus on the two strongest absorption components that are detected in  $\text{CO}(J=0 \rightarrow 1)$ .

The estimated  $\text{H}_2$  column densities traced by these two strong absorption components are  $N_{\text{H}_2} \gtrsim 3 \times 10^{20} \text{ cm}^{-2}$  (Section 4.1.1). The average volume densities of molecular clouds have been found to vary from roughly 1 to  $1000 \text{ cm}^{-3}$  (e.g., Smith et al. 2000; Heiner et al. 2008; Benincasa et al.

2013; Schneider et al. 2022), with densities reaching  $\sim 10^{4-5} \text{ cm}^{-3}$  at the threshold for star formation (e.g., Lada et al. 2010; Benincasa et al. 2013; Baade et al. 2024). If a single molecular cloud along the line of sight toward the background radio continuum causes an absorption component, and we assume a traditional estimate of the volume density of  $n_{\text{H}_2} \sim 150 \text{ cm}^{-3}$  (Scoville & Solomon 1975), then the diameter of this cloud would be  $D \sim 0.7 \text{ pc}$ , with a lower limit to the mass of  $M_{\text{H}_2} \gtrsim 1 M_{\odot}$ . It is likely that local volume densities are higher and the cloud diameter smaller, because we detect the absorption components also in CN, which has an effective density of order  $\gtrsim 10^4 \text{ cm}^{-2}$  (Shirley 2015). This is a very simplistic view, given that molecular clouds are complex systems, with often highly structured, filamentary, or even fractal characteristics (e.g., Elmegreen & Falgarone 1996; Combes 1998; Goldsmith et al. 2008; Men’shchikov et al. 2010; Heyer & Dame 2015; Schisano et al. 2020; Wong et al. 2022; Fahrion & De Marchi 2023; Li et al. 2023). Nevertheless, it serves to illustrate that the absorption in B2 0902+34 likely originates from small ( $\lesssim 1 \text{ pc}$ ) clouds rather than giant ( $\sim 10\text{--}100 \text{ pc}$ ) molecular cloud complexes.

A single cloud likely has a velocity dispersion ( $\sigma$ ) of order a few kilometers per second (Solomon et al. 1987; Benincasa et al. 2013; Miville-Deschênes et al. 2017; Spilker et al. 2022). This is significantly smaller than the FWHM  $\sim 26\text{--}69 \text{ km s}^{-1}$  ( $\sigma \sim 11\text{--}29 \text{ km s}^{-1}$ ) of the absorption components that we detect in B2 0902+34 (Table 1). This suggests that the absorption components may be caused by regions with many small clouds or cloud fragments (“cloudlets;” Gittins et al. 2003), where the overall kinematics are dominated by the velocity dispersion between the clouds. It is likely that the molecular clouds or cloudlets are optically thick, in which case their covering fraction of the background continuum is much less than 1. The crossing time of a cloud with a velocity of a few tens of kilometers per second and size  $\lesssim 1 \text{ pc}$  is short,  $t_{\text{cross}} \lesssim 10^5 \text{ yr}$ . This means that the clouds are likely short lived.

The absorption components that we detect in B2 0902+34 differ in CN abundance compared to CO (Figure 5). This could mean that the molecular gas structures are not uniform across the regions, and that perhaps high-density clouds or cloudlets are dispersed and mixed with lower-density molecular gas. This could represent a “cloudy region,” with many small and short-lived clumps covering a region that is highly turbulent. In such a region, cooling and dissipation would allow for the formation and growth of molecular clouds (e.g., Li & Bryan 2014a; Kanjilal et al. 2021), or the shattering of dense cold clouds could create a reservoir of diffuse and warmer molecular gas (e.g., Appleton et al. 2023).

The fact that absorption component 1 has approximately the same redshift as the previously detected HI absorber (Figure 4) suggests that the neutral gas likely also originates from the same region. However, the factor of three difference in line width between the deep CO absorption and the HI absorption (Figure 4) suggests that the cool neutral gas is even more turbulent than the ensemble of cold gas clouds. Again, this would suggest a region where dense, molecular gas clouds are embedded in a larger reservoir of more diffuse gas.

In the presence of a powerful radio source, such a region could have properties as predicted by precipitation models of many small cloudlets distributed throughout a larger reservoir of gas, where the formation and destruction of molecular

**Table 2**  
Existing Millimeter-band CO Detections

Source	$z_{\text{abs}}$	Type	$\int \tau_{\text{CO}} dv$	Trans.	Reference	$B_{\text{rest}}$	$K_{\text{rest}}$	$B - K$
0132-097	0.7634	I	75.6	1 $\rightarrow$ 2	W18	19.8	12.07	7.73
0201+113	3.3872	I	6.3	3 $\rightarrow$ 4	C23	18.66	15.16	3.50 <sup>a</sup>
0218+35	0.6885	I	20.3	1 $\rightarrow$ 2	W95	20.25	...	...
0902+34	3.398	A	5.35	0 $\rightarrow$ 1	this	21.80	17.61	4.19
1200+045	1.2128	A	3.1	1 $\rightarrow$ 2	C23	18.74	14.67	4.07
1245-19	1.2661	A	7.2	1 $\rightarrow$ 2	C23	...	16.55	...
1413+135	0.2467	A	3.6	0 $\rightarrow$ 1	W97	21.01	14.02	6.99
1504+37	0.6734	A	12.2	1 $\rightarrow$ 2	W96	21.44	14.66	6.78
1740-517	0.4423	A	4.8	1 $\rightarrow$ 2	A19	21.31	14.70	6.61
1830-211	0.8853	I	1.8	3 $\rightarrow$ 4	W98	22.98	...	...

**References:** W95: Wiklind & Combes (1995), W96: Wiklind & Combes (1996a), W97: Wiklind & Combes (1997), W98: Wiklind & Combes (1998), W18: Wiklind et al. (2018), A19: Allison et al. (2019), and C23: Combes & Gupta (2024).

**Note.**  $z_{\text{abs}}$  is the absorption redshift, followed by a flag designating whether this is associated with the continuum source (A) or arises in an intervening system (I). We then give the velocity-integrated optical depth of the CO absorption (in units of  $\text{km s}^{-1}$ ), the rotational transition to which this applies, and the reference. The last three columns give the rest-frame  $B$  and  $K$  magnitudes as well as the resulting rest-frame  $B - K$  color.

<sup>a</sup> This row is a tentative detection.

clouds is regulated through feedback (e.g., Sharma et al. 2010, 2012; Li & Bryan 2014b; Voit et al. 2015).

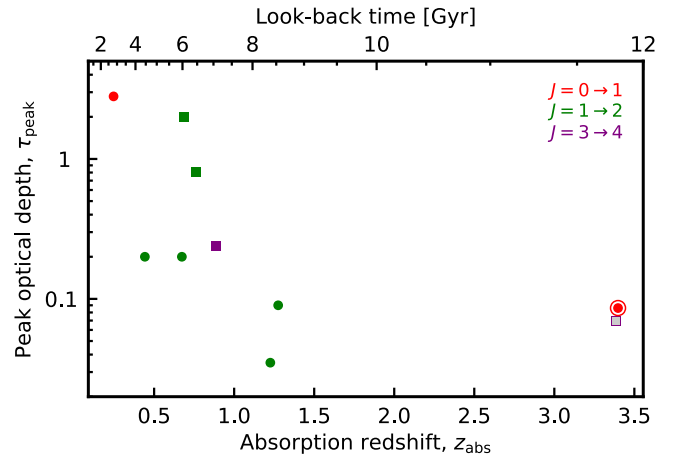
#### 4.2. Comparison to Previous CO Absorption Studies

Table 2 gives an overview of the 10 CO absorbers detected at  $z > 0.1$  (see Section 1). As shown in Figure 6, the CO absorption in B2 0902+34 is the highest-redshift example yet detected, possibly by a large margin. It is comparable in redshift only to the tentative detection of intervening CO ( $J = 3 \rightarrow 4$ ) absorption toward 0201+113, and its look-back time of almost 12 Gyr is at least 3 Gyr earlier than the other known CO absorbers.

As discussed in Section 1, there has been a lack of CO absorbers against bright radio-continuum sources at high and intermediate redshifts, despite dedicated searches. The high redshift of B2 0902+34 allows detection by the VLA, which has a high sensitivity in comparison with the millimeter-band telescopes used previously. However, the integrated signal of the CO absorption in B2 0902+34 is detected at a level  $\sim 45\sigma$  after 18.7 hr of on-source integration time. This means that the absorption signal would be detectable with the VLA at a  $5\sigma$  level after only an  $\sim 14$  minutes on-source exposure time, which is similar to the sensitivity of previous searches for CO absorption in radio sources at  $z > 1$  (e.g., Curran et al. 2011b). We therefore do not expect that the high sensitivity of our VLA observations introduced a bias or prevents a fair comparison with previous CO absorption studies in terms of detectability of the signal.

##### 4.2.1. Reddening versus Absorption Strength

Curran et al. (2006) noted that the sight-lines of damped Ly $\alpha$  absorption (DLA) systems, which have molecular fractions  $\mathcal{F} \equiv \frac{2N_{\text{H}_2}}{2N_{\text{H}_2} + N_{\text{HI}}} \sim 10^{-7}$ –0.3, appeared to be much less reddened, with optical to near-infrared colors of  $V - K \lesssim 4$ , than the millimeter-band absorbers, which have  $\mathcal{F} \approx 0.6$ –1 and  $V - K \gtrsim 5$ . That is, the millimeter-band detections occur along much redder and optically fainter sight-lines, suggesting dustier, more molecular-rich gas. Thus, targeting sight-lines toward sources that are sufficiently unobscured in the optical band, which can yield a reliable redshift to which to tune the millimeter receivers, will lead to a bias against the detection of



**Figure 6.** The observed peak optical depth of the CO absorption vs. the redshifts for all the known redshifted CO absorbers (Table 2). The dots and squares represent the associated and intervening absorbers, respectively. The circled red dot represents B2 0902+34. The purple-outlined gray square is the tentative CO ( $J = 3 \rightarrow 4$ ) absorption toward 0201+113 (Combes & Gupta 2024).

the cold, obscuring gas traced in the millimeter band (see also Zwaan & Prochaska 2006). In fact, all but one of the previous CO absorption detections were follow-up observations of targets that had previously been detected in HI 21 cm absorption (Uson et al. 1991; Carilli et al. 1992, 1998; Chengalur et al. 1999; Kanekar & Briggs 2003; Kanekar et al. 2003; Allison et al. 2019),<sup>15</sup> which is also correlated with the  $V - K$  color (Curran et al. 2019).

To test whether the absorption-line strength is consistent with the degree of reddening for B2 0902+34 and the other previous millimeter-band detections, Figure 7 shows the distributions of integrated optical depths and rest-frame  $B - K$  colors for the known detections of CO absorption at  $z_{\text{abs}} > 0.1$ . The colors were obtained following the procedure described in Appendix B and are listed for the detections in Table 2. Included in Figure 7 are the upper limits from the unsuccessful searches for redshifted CO absorption, as

<sup>15</sup> The exception is PKS 1830-211, which was found through a 14 GHz wide spectral scan of the 3 mm band (Wiklind & Combes 1996b).



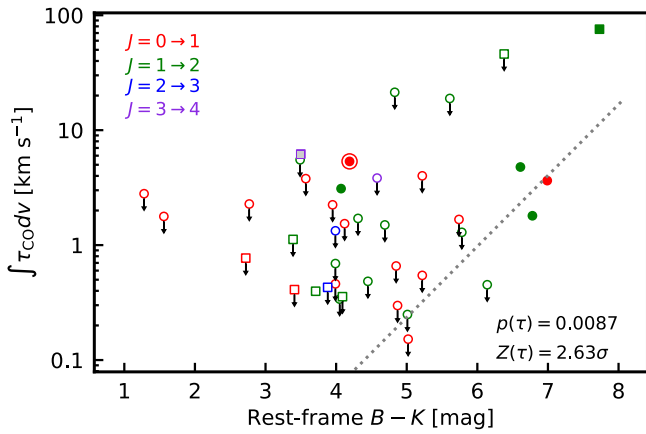


**Figure 7.** The velocity-integrated optical depth of the CO absorption plotted against the rest-frame  $B - K$  color of the sight-line. The associated systems are shown as circles and the intervening systems as squares. The circled red dot represents B2 0902+34. The unfilled symbols/arrows show the upper limits, which were calculated based on the  $3\sigma$  limit across a single channel with a width of  $10 \text{ km s}^{-1}$  (based on Curran et al. 2011b). These upper limits are included in the linear fit, shown by the dotted line. The statistics used to calculate the linear fit exclude 0201+113 (purple-gray square at  $B - K = 3.5$ ,  $\int \tau_{\text{CO}} dv = 6.3$ ) for reasons clarified in the text.

summarized in Curran et al. (2011b), with the addition of those in Combes & Gupta (2024).

For the CO detections, there are only seven sources with available colors. One of these is the intervening CO absorber toward PKS 0201+113 (purple-gray square at  $B - K = 3.5$ ,  $\int \tau_{\text{CO}} dv = 6.3$  in Figure 7), which was detected at a tentative  $3\sigma$  level (Combes & Gupta 2024). Furthermore, this absorber occurs in a DLA system with a low molecular fraction ( $6.3 \times 10^{-7} \leq \mathcal{F} \leq 2.5 \times 10^{-5}$ ; Srianand et al. 2012)<sup>16</sup> and so it is very anomalous. We therefore exclude 0201+113 from our statistics. The remaining six CO absorbers do not show evidence of a correlation. However, when adding the limits of the nondetections, via the Astronomy SURVival Analysis (ASURV) package (Isobe et al. 1986), a generalized nonparametric Kendall- $\tau$  test gives a probability of  $P(\tau) = 0.009$  of the distribution occurring by chance, which is significant at  $Z(\tau) = 2.63\sigma$ , assuming Gaussian statistics (see Table 3 of Appendix C). For this, the linear fit, including the limits, gives:

$$\log_{10} \int \tau_{\text{CO}} dv \approx 0.62(B - K) - 3.72. \quad (2)$$

Most of the published limits are in associated systems. Although four of the detected systems occur in absorbers intervening a more distant continuum source, the  $B - K$  color is only available for two of those, including 0201+113 (Table 2). The other intervening absorber is 0132–097, which constitutes an “end point” that drives the correlation, with the largest absorption strength and degree of reddening (the green square at  $B - K = 7.7$ ,  $\int \tau_{\text{CO}} dv = 76$  in Figure 7). Removing also this intervening system gives a significance of  $1.71\sigma$ .

Figure 7 shows that B2 0902+34 appears to be an outlier, being much less reddened ( $B - K \sim 4.2$ ) than would be expected based on the linear fit. This is also the case for the CO absorber toward 1200+045 at  $z = 1.2$  (Combes & Gupta 2024). However, the color of B2 0902+34 is quite

uncertain (see Appendix A).<sup>17</sup> Also, the different CO transitions shown in Figure 7 likely trace molecular gas with different excitation conditions, which may introduce scatter. Nevertheless, as more data are added, it would be interesting to see if the above fit, or any in Table 3 (Appendix C), provides a useful diagnostic in predicting the CO absorption-line strength from the sight-line color, as can be expected if both properties depend on the galaxy’s dust content.

## 5. Conclusions

We presented a multicomponent molecular absorption system in the radio galaxy B2 0902+34 at  $z = 3.4$ , detected in CO( $J = 0 \rightarrow 1$ ) and CN( $N = 0 \rightarrow 1$ ). This system was previously detected also in HI 21 cm absorption of neutral gas. The following summarizes the main results:

1. B2 0902+34 is the highest-redshift galaxy in which absorption of neutral and molecular gas has been detected.
2. The CO( $J = 0 \rightarrow 1$ ) absorption consists of two components, each tracing an  $\text{H}_2$  column density of  $N_{\text{H}_2} \gtrsim 3 \times 10^{20} \text{ cm}^{-2}$ . Combined with the large FWHM of the CO components (26 and  $69 \text{ km s}^{-1}$ ), we discuss the scenario that the absorption likely originates from a collection of small (parsec scale) molecular clouds that are distributed across a region with also diffuse gas and high turbulence among the clouds.
3. The CN( $N = 0 \rightarrow 1$ ) absorption consists of three components, with CO/CN ratios of integrated optical depth ranging from  $\lesssim 0.4$ –2.4. This suggests that the molecular clouds are dense ( $n_{\text{H}_2} \gtrsim 10^4 \text{ cm}^{-3}$ ) and likely irradiated by UV or X-ray emission, possibly near the central AGN or starburst region.
4. Compared to other distant CO absorbers and the large number of CO nondetections in the literature, we find indications at the  $2.6\sigma$  level for a correlation between the absorption-line strength and the rest-frame  $B - K$  color, with  $\log_{10} \int \tau_{\text{CO}} dv \approx 0.62(B - K) - 3.72$ . If confirmed, this could indicate that detectable CO absorption is more prevalent among galaxies with a higher dust content. Despite this, B2 0902+34 shows less red colors than the CO absorption systems at  $z < 1$ .

As a result of our VLA observations, the discovery of this multiphase absorber, 1.5 Gyr after the Big Bang, opens a window for studying the neutral and molecular gas on small scales in distant galaxies during the era of the Square Kilometre Array (Lazio 2009) and Next-Generation Very Large Array (Murphy 2018).

## Acknowledgments

The authors thank Ilse van Bommel and Suma Murthy for useful discussions. The National Radio Astronomy Observatory is a facility of the National Science Foundation operated under cooperative agreement by Associated Universities, Inc. Based on observations with the NASA/ESA Hubble Space Telescope obtained from the Data Archive at the Space Telescope Science Institute, which is operated by the Association of Universities for Research in Astronomy, Incorporated, under NASA contract NAS5-26555. Support for program number HST-GO-17268 was provided through a grant from the STScI under National Aeronautics and Space Administration

<sup>16</sup> As would be expected from its low metallicity of  $[Z/H] = -1.26$  (Curran et al. 2004).

<sup>17</sup> Removing B2 0902+34, in addition to 0201+113, increases the significance of the correlation to  $Z(\tau) = 2.90\sigma$  (see Table 3 of Appendix A).

(NASA) contract NAS5-26555. R.J.v.W. acknowledges support from the ERC Starting Grant ClusterWeb 804208. M.V.M. acknowledges support from grant PID2021-124665NB-I00 by the Spanish Ministry of Science and Innovation (MCIN)/State Agency of Research (AEI)/10.13039/501100011033 and by the European Regional Development Fund (ERDF) “A way of making Europe.”

*Facilities:* VLA and HST.

*Software:* CASA (CASA Team et al. 2022).

## Appendix A CO Spectrum Prior to Continuum Subtraction

Section 2 described why and how the radio continuum was subtracted in the  $(u, v)$  domain prior to imaging the line data. Figure 8 shows the  $\text{CO}(J=0 \rightarrow 1)$  absorption on top of the continuum in the image cube that was made prior to continuum subtraction. This illustrates that the continuum subtraction had no adverse effect on the absorption signal.

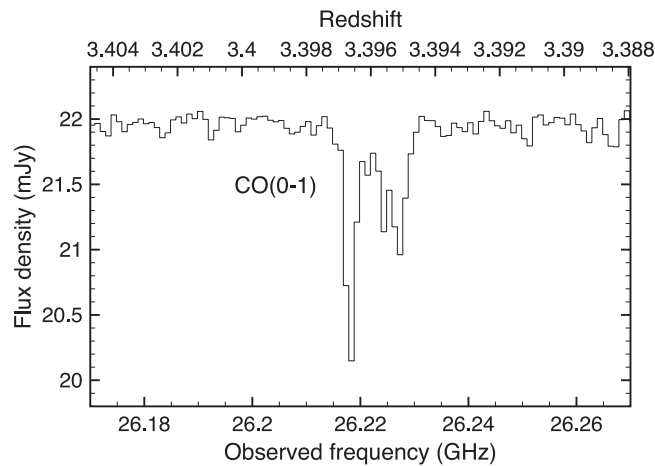


**Figure 8.**  $\text{CO}(J=0 \rightarrow 1)$  absorption spectrum superposed on top of the radio continuum. This spectrum was obtained from an image cube made before subtracting the continuum in the  $(u, v)$  domain (Section 2).

## Appendix B

### Sight-line Colors to CO Absorbers

In order to test whether the absorption-line strength of  $\int \tau d\nu = 5.35 \text{ km s}^{-1}$  is consistent with the degree of reddening (Section 4.2.1) for B2 0902+34 and the other previous detections and nondetections, we used the same method as Curran & Moss (2019), where we scraped the photometry from the NASA/IPAC Extragalactic Database (NED), the Wide-Field Infrared Survey Explorer (WISE; Wright et al. 2010), and the Two Micron All Sky Survey (2MASS; Skrutskie et al. 2006).

Figure 9 shows the broadband photometry from NED, WISE, and 2MASS of all known CO absorbers at  $z > 0.1$ . Given the large redshift of B2 0902+34, we shifted the SEDs back into the rest frame. Following the same method as Curran (2021), if the frequency of the photometric point fell within  $\Delta \log_{10} \nu = \pm 0.05$  of the central frequency of the band, the flux measurement was added with multiple values being averaged. If no photometry for that band was available, this was obtained by a power-law fit to the neighboring photometric points. Results of the color analysis of the CO absorbers are summarized in Table 2 and further details are provided in Section 4.2.1.

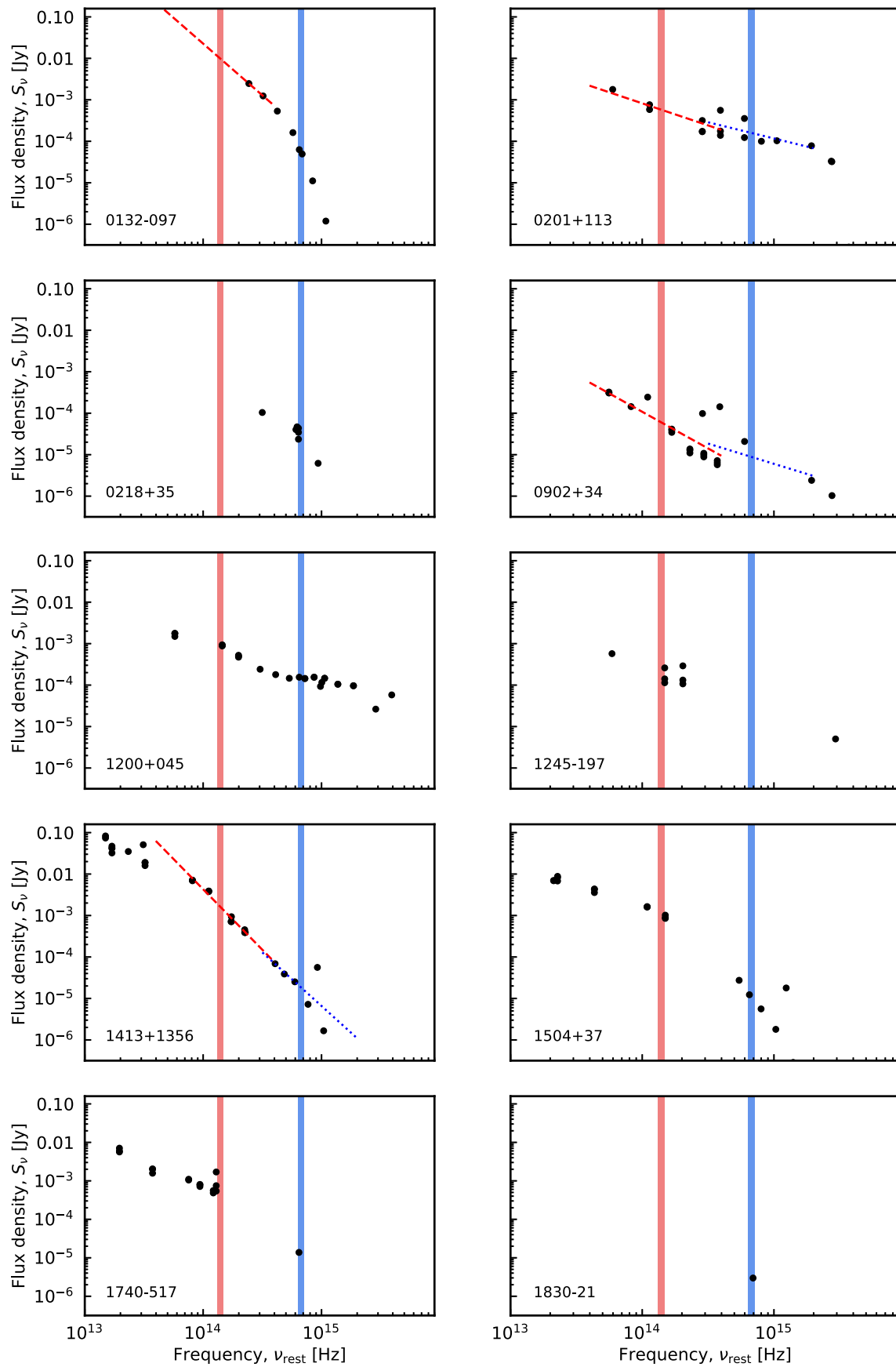


**Figure 9.** The optical and near-infrared photometry in the rest frame of the absorber, for the sources detected in redshifted CO absorption. The lines show the power-law fits used to obtain the  $K$  (red dashed) and  $B$  magnitudes (blue dotted), where these did not fall into the bands. Results are summarized in Table 2.

### Appendix C Statistics on Correlation between Absorption Strength and $B - K$ Color

Table 3 gives an overview of the statistics of the CO absorption strength versus rest-frame  $B - K$  color for both the detections (Table 2) and nondetections (Curran et al. 2011b;

Combes & Gupta 2024). This follows the analysis shown in Appendix B and the equation:

$$\log_{10} \int \tau_{\text{CO}} dv = m \cdot (B - K) + c, \quad (\text{C1})$$








where  $m$  is the gradient and  $c$  is the intercept of the linear fit. See Table 3 for more details.

**Table 3**  
Statistics of the CO Absorption Strength versus Rest-frame  $B - K$  Color of the Sight-line (Figure 7)

Sample	$n$	$p(\tau)$	$Z(\tau)$	$m$	$c$
WHOLE SAMPLE					
Detections	7	0.881	$0.15\sigma$	0.10	0.81
All	40	0.050	$1.96\sigma$	0.48	-2.89
Associated only	31	0.098	$1.66\sigma$	0.35	-2.22
EXCLUDING 0201+113					
Detections	6	0.573	$0.56\sigma$	0.16	-0.19
All	39	0.009	$2.63\sigma$	0.62	-3.72
Associated only	31	0.098	$1.66\sigma$	0.35	-2.22
EXCLUDING 0201+113 AND B2 0902+34					
Detections	5	0.327	$0.98\sigma$	0.23	-0.72
All	38	0.004	$2.90\sigma$	0.73	-4.45
Associated only	30	0.033	$2.14\sigma$	0.47	-2.94

**Note.** Statistics are given for the whole sample, the sample excluding 0201+113, the sample excluding 0201+113 and B2 0902+34, and the associated absorbers only.  $n$  gives the sample size,  $p(\tau)$  and  $Z(\tau)$  the results of a Kendall- $\tau$  test and  $m$  &  $c$  the gradient and intercept of the linear fit, respectively (see main text).

## ORCID iDs

Bjorn H. C. Emonts  <https://orcid.org/0000-0003-2983-815X>  
 Steve J. Curran  <https://orcid.org/0000-0002-1163-010X>  
 George K. Miley  <https://orcid.org/0000-0003-2884-7214>  
 Matthew D. Lehnert  <https://orcid.org/0000-0003-1939-5885>  
 Chris L. Carilli  <https://orcid.org/0000-0001-6647-3861>  
 Ilsang Yoon  <https://orcid.org/0000-0001-9163-0064>  
 Raffaella Morganti  <https://orcid.org/0000-0002-9482-6844>  
 Reinout J. van Weeren  <https://orcid.org/0000-0002-0587-1660>  
 Montserrat Villar-Martín  <https://orcid.org/0000-0003-2566-2126>  
 Pierre Guillard  <https://orcid.org/0000-0002-2421-1350>  
 Cristina M. Cordun  <https://orcid.org/0009-0003-5974-0185>  
 Tom A. Oosterloo  <https://orcid.org/0000-0002-0616-6971>

## References

- Aalto, S., Polatidis, A. G., Hüttemeister, S., et al. 2002, *A&A*, 381, 783  
 Adams, J. J., Hill, G. J., & MacQueen, P. J. 2009, *ApJ*, 694, 314  
 Allison, J. R., Mahony, E. K., Moss, V. A., et al. 2019, *MNRAS*, 482, 2934  
 Appleton, P. N., Guillard, P., Emonts, B., et al. 2023, *ApJ*, 951, 104  
 Baade, J. C., Kong, S., Bieging, J. H., & Folkers, T. 2024, *ApJ*, 960, 33  
 Balashev, S. A., Klimenko, V. V., Ivanchik, A. V., et al. 2014, *MNRAS*, 440, 225  
 Balashev, S. A., & Noterdaeme, P. 2018, *MNRAS*, 478, L7  
 Benincasa, S. M., Tasker, E. J., Pudritz, R. E., et al. 2013, *ApJ*, 776, 23  
 Boger, G. I., & Sternberg, A. 2005, *ApJ*, 632, 302  
 Bolatto, A. D., Wolfire, M., & Leroy, A. K. 2013, *ARA&A*, 51, 207  
 Briggs, F. H., Sorar, E., & Taramopoulos, A. 1993, *ApJL*, 415, L99  
 Brooke, J. S. A., Ram, R. S., Western, C. M., et al. 2014, *ApJS*, 210, 23  
 Carilli, C. L. 1995, *A&A*, 298, 77  
 Carilli, C. L., Menten, K. M., Reid, M. J., et al. 1998, *ApJ*, 494, 175  
 Carilli, C. L., Menten, K. M., Stocke, J. T., et al. 2000, *PhRvL*, 85, 5511  
 Carilli, C. L., Perlman, E. S., & Stocke, J. T. 1992, *ApJL*, 400, L13  
 CASA Team, Bean, B., Bhatnagar, S., et al. 2022, *PASP*, 134, 114501  
 Chandra, P., Swarup, G., Kulkarni, V. K., et al. 2004, *JApA*, 25, 57  
 Chandra, S., Maheshwari, V. U., & Sharma, A. K. 1996, *A&AS*, 117, 557  
 Chengalur, J. N., de Bruyn, A. G., & Narasimha, D. 1999, *A&A*, 343, L79  
 Cicone, C., Maiolino, R., Aalto, S., et al. 2020, *A&A*, 633, A163  
 Cody, A. M., & Braun, R. 2003, *A&A*, 400, 871  
 Combes, F. 1998, *CeMDA*, 72, 91  
 Combes, F. 2008, *Ap&SS*, 313, 321  
 Combes, F., & Gupta, N. 2024, *A&A*, in press (arXiv:2310.17204)  
 Combes, F., Gupta, N., Jozsa, G. I. G., et al. 2019, *A&A*, 623, A133  
 Combes, F., & Wiklind, T. 1997, *ApJL*, 486, L79  
 Cordun, C. M., Timmerman, R., Miley, G. K., et al. 2023, *A&A*, 676, A29  
 Curran, S. J. 2021, *MNRAS*, 508, 1165  
 Curran, S. J., Hunstead, R. W., Johnston, H. M., et al. 2019, *MNRAS*, 484, 1182  
 Curran, S. J., & Moss, J. P. 2019, *A&A*, 629, A56  
 Curran, S. J., Tanna, A., Koch, F. E., et al. 2011a, *A&A*, 533, A55  
 Curran, S. J., Webb, J. K., Murphy, M. T., et al. 2004, *MNRAS*, 351, L24  
 Curran, S. J., Whiting, M. T., Combes, F., et al. 2011b, *MNRAS*, 416, 2143  
 Curran, S. J., Whiting, M. T., Murphy, M. T., et al. 2006, *MNRAS*, 371, 431  
 Curran, S. J., Whiting, M. T., Wiklind, T., et al. 2008, *MNRAS*, 391, 765  
 da Cunha, E., Groves, B., Walter, F., et al. 2013, *ApJ*, 766, 13  
 Dessauges-Zavadsky, M., Richard, J., Combes, F., et al. 2023, *MNRAS*, 519, 6222  
 Drinkwater, M. J., Combes, F., & Wiklind, T. 1996, *A&A*, 312, 771  
 Eales, S., Rawlings, S., Puxley, P., et al. 1993, *Natur*, 363, 140  
 Elmegreen, P., & Dickinson, M. 1992, *ApJL*, 399, L47  
 Elmegreen, B. G., & Falgarone, E. 1996, *ApJ*, 471, 816  
 Evans, A. S., Sanders, D. B., Mazzarella, J. M., et al. 1996, *ApJ*, 457, 658  
 Fabian, A. C., Crawford, C. S., & Iwasawa, K. 2002, *MNRAS*, 331, L57  
 Fahion, K., & De Marchi, G. 2023, *A&A*, 681, A20  
 Frerking, M. A., Langer, W. D., & Wilson, R. W. 1982, *ApJ*, 262, 590  
 Fuente, A., Martín-Pintado, J., & Gaume, R. 1995, *ApJL*, 442, L33  
 García-Burillo, S., Usero, A., Fuente, A., et al. 2010, *A&A*, 519, A2  
 Gerin, M., Phillips, T. G., Benford, D. J., et al. 1997, *ApJL*, 488, L31  
 Gittins, D. M., Clarke, C. J., & Bate, M. R. 2003, *MNRAS*, 340, 841  
 Godard, B., Pineau des Forêts, G., Lesaffre, P., et al. 2019, *A&A*, 622, A100  
 Goldsmith, P. F., Heyer, M., Narayanan, G., et al. 2008, *ApJ*, 680, 428  
 Guszejnov, D., Grudić, M. Y., Offner, S. S. R., et al. 2020, *MNRAS*, 492, 488  
 Heiner, J. S., Allen, R. J., Emonts, B. H. C., et al. 2008, *ApJ*, 673, 798  
 Heyer, M., & Dame, T. M. 2015, *ARA&A*, 53, 583  
 Hodge, J. A., Carilli, C. L., Walter, F., et al. 2012, *ApJ*, 760, 11  
 Isobe, T., Feigelson, E., & Nelson, P. 1986, *ApJ*, 306, 490  
 Kanekar, N., & Briggs, F. H. 2003, *A&A*, 412, L29  
 Kanekar, N., Chengalur, J. N., de Bruyn, A. G., et al. 2003, *MNRAS*, 345, L7  
 Kanekar, N., Chengalur, J. N., & Lane, W. M. 2007, *MNRAS*, 375, 1528  
 Kanekar, N., Gupta, A., Carilli, C. L., et al. 2014, *ApJ*, 782, 56  
 Kanjilal, V., Dutta, A., & Sharma, P. 2021, *MNRAS*, 501, 1143  
 Kazandjian, M. V., Meijerink, R., Pelupessy, I., et al. 2015, *A&A*, 574, A127  
 Klitsch, A., Péroux, C., Zwaan, M. A., et al. 2019, *MNRAS*, 490, 1220  
 Lada, C. J., Lombardi, M., & Alves, J. F. 2010, *ApJ*, 724, 687  
 Lazio, J. 2009, in Proc. of Panoramic Radio Astronomy 89, Wide-field 1-2 GHz Research on Galaxy Evolution, 58  
 Lehmann, A., Godard, B., Pineau des Forêts, G., et al. 2022, *A&A*, 658, A165  
 Lepp, S., & Dalgarno, A. 1996, *A&A*, 306, L21  
 Levshakov, S. A., & Varshalovich, D. A. 1985, *MNRAS*, 212, 517  
 Li, X.-M., Zhang, G.-Y., Men'shchikov, A., et al. 2023, *A&A*, 674, A225  
 Li, Y., & Bryan, G. L. 2014a, *ApJ*, 789, 153  
 Li, Y., & Bryan, G. L. 2014b, *ApJ*, 789, 54  
 Lilly, S. J. 1988, *ApJ*, 333, 161  
 Maccagni, F. M., Morganti, R., Oosterloo, T. A., et al. 2018, *A&A*, 614, A42  
 Mangum, J. G., & Shirley, Y. L. 2015, *PASP*, 127, 266  
 Meijerink, R., Spaans, M., & Israel, F. P. 2007, *A&A*, 461, 793  
 Men'shchikov, A., André, P., Didelon, P., et al. 2010, *A&A*, 518, L103  
 Miville-Deschênes, M.-A., Murray, N., & Lee, E. J. 2017, *ApJ*, 834, 57  
 Morganti, R., Murthy, S., Guillard, P., et al. 2023, *Galax*, 11, 24  
 Morganti, R., & Oosterloo, T. 2018, *A&ARv*, 26, 4  
 Muller, S., Beelen, A., Black, J. H., et al. 2013, *A&A*, 551, A109  
 Muller, S., Beelen, A., Guélin, M., et al. 2011, *A&A*, 535, A103  
 Muller, S., Combes, F., Guélin, M., et al. 2014, *A&A*, 566, A112  
 Muller, S., Martí-Vidal, I., Combes, F., et al. 2023, *A&A*, 674, A101  
 Muller, S., Ubachs, W., Menten, K. M., et al. 2021, *A&A*, 652, A5  
 Murphy, E. 2018, in ASP Conf. Ser. 517, Science with a Next Generation Very Large Array  
 Murphy, M. T., Curran, S. J., & Webb, J. K. 2003, *MNRAS*, 342, 830  
 Noterdaeme, P., Srikanand, R., Rahmani, H., et al. 2015, *A&A*, 577, A24  
 Osterbrock, D. E. 1989, *Astrophysics of Gaseous Nebulae and Active Galactic Nuclei* (Mill Valley, CA: Univ. Science Books), 408  
 Oteo, I., Zwaan, M. A., Ivison, R. J., et al. 2016, *ApJ*, 822, 36  
 Pearson, T. J., & Readhead, A. C. S. 1984, *ARA&A*, 22, 97  
 Pentericci, L., Röttgering, H. J. A., Miley, G. K., et al. 1999, *A&A*, 341, 329  
 Ranjan, A., Noterdaeme, P., Krogager, J.-K., et al. 2018, *A&A*, 618, A184  
 Reuland, M., van Breugel, W., Röttgering, H., et al. 2003, *ApJ*, 592, 755  
 Riechers, D. A., Walter, F., Cox, P., et al. 2007, *ApJ*, 666, 778  
 Riechers, D. A., Weiss, A., Walter, F., et al. 2022, *Natur*, 602, 58  
 Rose, T., Edge, A. C., Combes, F., et al. 2019, *MNRAS*, 485, 229  
 Rose, T., McNamara, B. R., Combes, F., et al. 2023, *MNRAS*, 518, 878  
 Schisano, E., Molinari, S., Elia, D., et al. 2020, *MNRAS*, 492, 5420  
 Schneider, N., Ossenkopf-Okada, V., Clarke, S., et al. 2022, *A&A*, 666, A165  
 Scoville, N. Z., & Solomon, P. M. 1975, *ApJL*, 199, L105  
 Sharma, P., McCourt, M., Quataert, E., et al. 2012, *MNRAS*, 420, 3174  
 Sharma, P., Parrish, I. J., & Quataert, E. 2010, *ApJ*, 720, 652  
 Shirley, Y. L. 2015, *PASP*, 127, 299  
 Skrutskie, M. F., et al. 2006, *AJ*, 131, 1163  
 Smith, D. A., Allen, R. J., Bohlin, R. C., et al. 2000, *ApJ*, 538, 608  
 Solomon, P. M., Rivolo, A. R., Barrett, J., et al. 1987, *ApJ*, 319, 730  
 Spilker, A., Kainulainen, J., & Orkisz, J. 2022, *A&A*, 667, A110  
 Srikanand, R., Gupta, N., Petitjean, P., et al. 2012, *MNRAS*, 421, 651  
 Sternberg, A., & Dalgarno, A. 1995, *ApJS*, 99, 565  
 Uson, J. M., Bagri, D. S., & Cornwell, T. J. 1991, *PhRvL*, 67, 3328  
 van Ojik, R., Roettgering, H. J. A., van der Werf, P. P., et al. 1997, *A&A*, 321, 389  
 Voit, G. M., Donahue, M., Bryan, G. L., et al. 2015, *Natur*, 519, 203  
 Wakelam, V., Loison, J.-C., Herbst, E., et al. 2015, *ApJS*, 217, 20  
 Wiklind, T., & Combes, F. 1995, *A&A*, 299, 382  
 Wiklind, T., & Combes, F. 1996a, *A&A*, 315, 86  
 Wiklind, T., & Combes, F. 1996b, *Nat*, 379, 139  
 Wiklind, T., & Combes, F. 1997, *A&A*, 328, 48  
 Wiklind, T., & Combes, F. 1998, *ApJ*, 500, 129  
 Wiklind, T., & Combes, F. 1999, in ASP Conf. Ser. 156, Highly Redshifted Radio Lines, ed. C. L. Carilli, 202

- Wiklind, T., Combes, F., & Kanekar, N. 2018, [ApJ](#), 864, 73
- Wilson, C. D. 2018, [MNRAS](#), 477, 2926
- Wilson, C. D., Walker, C. E., & Thornley, M. D. 1997, [ApJ](#), 483, 210
- Wilson, T. L., Rohlfs, K., & Hüttemeister, S. 2013, *Tools of Radio Astronomy* (Berlin: Springer)
- Wong, T., Oudshoorn, L., Sofovich, E., et al. 2022, [ApJ](#), 932, 47
- Wright, E. L. 2006, [PASP](#), 118, 1711
- Wright, E. L., Eisenhardt, P. R. M., Mainzer, A. K., et al. 2010, [AJ](#), 140, 1868
- Zhang, Z.-Y., Papadopoulos, P. P., Ivison, R. J., et al. 2016, [RSOS](#), 3, 160025
- Zwaan, M. A., & Prochaska, J. X. 2006, [ApJ](#), 643, 675